SAND2022-0105C

A robust framework for the simulation of scalar transport in turbulent spray combustion

Everett A Wenzel[a,*], Mustafa Kaddoura[b], Sean C Garrick[c]

[a] *Sandia National Laboratories*
[b] *Deparment of Mechanical Engineering, University of Minnesota - Twin Cities*
[c] *Mechanical Science & Engineering, University of Illinois - Urbana Champaign*

Abstract

Spray combustion involves many processes, including phase change, heat and mass transfer, and chemical reaction. Accurate modeling of these systems requires computational methods capable of providing low dissipation and bounded transport of scalars, including species mass fractions and temperature. Methods appropriate for use in engineering applications typically fail to provide low dissipation, bounded transport near phase interfaces, where fluid properties are discontinuous. In this work, we present a scalar transport method based upon the Eulerian-Lagrangian point mass particle – a framework previously applied to immiscible phase transport. Concepts from smooth particle hydrodynamics are leveraged to compute diffusion rates, while the point mass particle motion accounts for scalar advection. The formulation is presented in the context of heat transfer, and verification is performed for interfacial diffusion and single phase advection-diffusion. The paper concludes by demonstrating multiphase heat transfer between a rising gas bubble in liquid, and a high Reynolds number temporal mixing layer. The results demonstrate the method to provide low dissipation, bounded, and conservative scalar transport.

Keywords: scalar transport; multiphase; heat transfer; turbulence.

1. Introduction

Liquid fuel combustion involves numerous interdependent processes, including atomization, interfacial heat transfer and phase change, mass diffusion, chemical reaction, and particle nucleation and growth. These processes generate large gradients in important scalar fields, including temperature and species mass fraction. Discontinuous fluid properties at phase interfaces introduce the additional complication of discontinuous gradients. Heat and mass transfer near phase interfaces controls the rate of phase change, which strongly influences combustion efficiency and exhaust gas composition [1, 2]. An understanding of the near-interface heat and mass transfer is therefore required to inform engineering designs.

Modeling and simulation of the spray combustion environment involves many unsolved or underdeveloped problems: performing consistent transport of advected quantities (that is, using the same numerical operators to transport conserved quantities) [3, 4]; maintaining boundedness of scalar quantities [5]; minimizing numerical dissipation at low numerical resolutions, and resolving or modeling all relevant spatio-temporal scales. These challenges are amplified for spray combustion, as an immiscible multiphase process, because a phase capturing methodology is required to inform the local phase, which may or may not be conservative, affordable, amenable to consistent transport, or applicable to unstructured meshes. Engineering efforts to improve combustion systems therefore require improved methods to address the current shortcomings [5].

The coupled Eulerian-Lagrangian point mass particle (ELPMP) method is a newly proposed simulation paradigm for simulating multiphase flows. The approach is characterized by simultaneous discretizations of the flow system by an Eulerian mesh and Lagrangian point mass particles (PMPs) [6, 7]. The ELPMP has been verified in the context of phase tracking [6], and has been proposed as a consistent and conservative framework for performing multiphase Direct Numerical Simulation and Large Eddy Simulation [7]. The ELPMP is novel in that a consistency constraint on the spatial distribution of the PMPs eliminates the need to re-mesh or re-seed the Lagrangian domain. The approach provides a number of advantages in the context of spray combustion: (1) advection via the PMP is consistent and conservative; (2) advected quantities remain bounded and suffer little diffusive error, even for poorly-resolved flow features (3) if desired, the PMPs can discretize the system at a finer resolution than the Eulerian mesh, and their behavior is independent of the mesh type.

This paper presents an approach for simulating multiphase heat transport in the context of the ELPMP. Although the discussion is limited to heat transfer, extension to any advection-diffusion equation is straight forward. Verification of the method is performed by assessing multiphase diffusion, and single phase advection-diffusion. Following the verification, multiphase capability is demonstrated via simulation of a hot bubble rising in liquid. Lastly, robustness in the context of turbulent flows is demonstrated by means of a high Reynolds number temporal mixing layer.

2. Formulation

The presented computational method directly extends the PMP-based phase tracking methodology of Wenzel and Garrick [6]. A complete description of this underlying method is beyond the present scope, and the curious reader is directed to [6]. Instead, this section begins with a sufficiently detailed summary of the ELPMP discretization to allow for the heat transfer extension to be presented in the later portion of the section.

2.1. Coupled Eulerian-Lagrangian point mass particle discretization

Consider a dynamic fluid system occupying region Ω at time $t = t^n$. Eulerian methods integrate the system in time to $t^{n+1} = t^n + \Delta t$ by: (1) discretizing the system mass, momentum, and energy with an Eulerian mesh; (2) evaluating fluxes as a function of the Eulerian discretization; and (3) evaluating the time integration as a function of the Eulerian fluxes. In the ELPMP paradigm, the Eulerian discretization is retained, but is supplemented by a simultaneous Lagrangian discretization of the same fluid system by N_p point mass particles (PMPs). The PMPs can provide a discretization for all conserved quantities or a subset of the conserved quantities, but must always discretize the system mass.

A discretization of the system mass by N_p PMPs at time $t = t^n$ is defined by applying two constraints. First, global mass conservation is enforced by assigning each PMP a mass M_i^n, such that

$$\int_\Omega \rho^n d\Omega = \sum_{i=1}^{N_p} M_i^n, \tag{1}$$

where ρ^n is the local fluid density at time t^n. Second, the spatial distribution of PMPs is constrained to be representative of the fluid density at all locations $\mathbf{x}$. The fluid density at point $\mathbf{x}$ is approximated by the Smoothed Particle Hydrodynamics (SPH) convolution expression,

$$\rho^n(\mathbf{x}) = \sum_{i=1}^{N_p} W\left(\mathbf{x} - \mathbf{X}_i^n, h\right) M_i^n, \tag{2}$$

where $\mathbf{X}_i^n$ is the position of particle i at time t^n, and h is the non-zero extent of the compact weight function W [8, 9]. Identifying particle masses M_i^n and positions $\mathbf{X}_i^n$ that satisfy Eq. (1) and Eq. (2) establishes the PMP discretization of mass at time t^n.

Advancement from time level n to $n+1$ is achieved by integrating the Eulerian solution, and by moving the PMPs according to

$$d\mathbf{X}_i^n = \mathbf{U}_i^n \Delta t, \tag{3}$$

where $\mathbf{U}_i^n$ is the PMP velocity. Because the Eulerian solution and the PMPs constitute simultaneous discretizations of the same fluid system, the PMP velocity $\mathbf{U}_i^n$ is constrained such that Eq. (1) and Eq. (2) are satisfied at time level $n+1$. An expression for the PMP velocity with this property has been derived through the following logic [6]: (1) express the PMP velocity as the sum of the interpolated Eulerian velocity $\overline{\mathbf{u}}_i$ and a residual velocity $\mathbf{u}_i'$; (2) express the PMP acceleration as a function of inter-particle forces computed in the SPH framework; (3) Taylor series expand the PMP velocity in time, substitute the inter-particle forces, and collapse time derivatives of the interpolated velocity. This procedure results in the following expression for the PMP velocity,

$$\mathbf{U}_i^n = \overline{\mathbf{u}}_i^n + \left(\mathbf{F}_i' + \mathbf{P}_i'\right)^n \Delta t + \mathbf{u}_i'^{n-1} + \mathcal{O}\left(\Delta t^2\right), \tag{4}$$

where $\mathbf{F}_i'$ and $\mathbf{P}_i'$ are residual inter-particle forces, and $\mathbf{u}_i'^{n-1}$ is the residual velocity from the previous time level. Further details regarding Eq. (4) and the corresponding closure model are provided by Wenzel and Garrick [6].

The ELPMP discretization of the system mass, defined by Eqs. (1-4), is extended to a phase tracking approach by associating each particle with a phase indicator χ_i. An Eulerian color function can then be computed from the particles via convolution, and used to inform the Eulerian properties and surface tension [6]. With this background, we develop an ELPMP discretization for the mass, phase, and thermal energy.

2.2. ELPMP discretization for thermal transport

Consider a field of N_p PMP particles that compose a discretization for the system mass, phase, and internal energy. The associated discretization constraint is given by

$$\int_\Omega \rho^n c^n T^n d\Omega = \sum_{i=1}^{N_p} c_i^n T_i^n M_i^n, \tag{5}$$

where c is the specific heat and T is the temperature. Advancing the particle temperature T_i^n forward in time requires the the Lagrangian form of the energy equation,

$$\frac{DT_i}{Dt} = \frac{1}{\rho_i c_i}\left[\nabla \cdot \mathrm{k} \nabla T\right]_i, \tag{6}$$

where the right-hand-side is the Lagrangian thermal diffusion operator evaluated for particle i, and k is the thermal conductivity. Because the PMP particles are advected with the PMP velocity, thermal advection is naturally accounted for, and is consistent with the transport of mass and phase information. A closure strategy for thermal diffusion is required to complete the model.

We adopt a thermal diffusion operator proposed by Cleary and Monaghan [10], which has been demonstrated in the context of SPH to accurately quantify diffusion across interfaces with discontinuous changes in fluid properties, including density, thermal conductivity, and specific heat. The diffusion operator is given by

$$\frac{1}{\rho_i c_i}\left[\nabla \cdot \mathrm{k} \nabla T\right]_i = \frac{1}{\rho_i c_i} \sum_{j=1}^{N_p} \frac{M_j}{\rho_j} \frac{4\mathrm{k}_i \mathrm{k}_j}{\mathrm{k}_i + \mathrm{k}_j} \left(T_i - T_j\right) \frac{\nabla W_{ij}^q}{\mathbf{X}_i - \mathbf{X}_j}, \tag{7}$$

where ρ_i and ρ_j are the densities of particles i and j evaluated with Eq. (2), respectively, and ∇W_{ij}^q is the gradient of a thermal weight function evaluated between particles i and j [10]. Heat diffusion occurs in a pair-wise fashion between particles, ensuring conservation. Equation (7) could be directly implemented for closure of Eq. (6). However, the present discussion is limited to constant density systems, and this allows for simplification. Instead of computing the particle density ρ_i on every particle for use in Eq. (7), we assign each particle density (and other fluid properties) according to the particle phase indicator value: if $\chi_i = 1$ corresponding to the liquid phase, then $\rho_i = \rho_l$, $\mathrm{k}_i = \mathrm{k}_l$, and $c_i = c_l$.

The thermal weight function used in this work is a modified version of the M_4 cubic spline [9],

$$M^q = \frac{1}{\pi h_q^3} \begin{cases} 0, & q < 0.1; \\ \frac{1}{4}\left(2-q\right)^3 - \left(1-q\right)^3, & 0.1 \le q < 1; \\ \frac{1}{4}\left(2-q\right)^3, & 1 \le q < 2; \\ 0, & q \ge 2, \end{cases} \tag{8}$$

where $q = \left|\mathbf{X}_i - \mathbf{X}_j\right| / h_q$, $h_q = 1.2 V_i^{1/3}$, and V_i is the volume of particle i. The above weight has been modified in that $M^q = 0$ for $q < 0.1$, which prevents heat exchange between particles that have become too close in proximity.

A consequence of prescribing the particle densities, rather than computing them via Eq. (2), is that the discrete normalization requirement for the weight function is not satisfied [11]. We therefore introduce a pre-factor to the weight, c_n, resulting in a new weight function that better satisfies the normalization criteria:

$$W^q\left(q\right) = c_n M^q\left(q\right). \tag{9}$$

In this work, we have implemented $c_n = 1.1$.

2.3. Time integration

An operator-split approach for time integration of temperature in the context of the ELPMP method is proposed as follows:

1. The thermal energy of the system is discretized by the PMPs at time level $n-1/2$, such that the distribution of thermal energy is defined by the particle temperature $T_i^{n-1/2}$, the particle mass M_i, and the particle position $\mathbf{X}_i^{n-1/2}$.
2. The position of each PMP i is advanced from time level $\mathbf{X}_i^{n-1/2}$ to time level $\mathbf{X}_i^{n+1/2}$ via the procedures outlined in Section 4.3.2 of [6]. This motion of the particles accounts for thermal advection.
3. The diffusion operator $\mathfrak{D}_i$ is computed for each particle i using the most up-to-date particle position $\mathbf{X}_i^{n+1/2}$ and the particle temperature $T_i^{n-1/2}$

$$\mathfrak{D}_i = \frac{1}{\rho_i c_i} \sum_{j=1}^{N_p} \frac{m_j}{\rho_j} \frac{4\mathrm{k}_i \mathrm{k}_j}{\mathrm{k}_i + \mathrm{k}_j} \times \left(T_i^{n-1/2} - T_j^{n-1/2}\right) \frac{\nabla W_{ij}^{q\ n+1/2}}{\mathbf{X}_i^{n+1/2} - \mathbf{X}_j^{n+1/2}}. \tag{10}$$

4. The temperature at time level $n+1/2$ is computed according to

$$T_i^{n+1/2} = T_i^{n-1/2} + \Delta t \mathfrak{D}_i. \tag{11}$$

3. Performance assessment

We assess the performance of the ELPMP approach via two verification tests and two demonstration problems. The verification tests examine multiphase conduction, and single phase advection & diffusion. After the verification tests, a warm bubble rising in liquid is presented, followed by a high Reynolds number temporal mixing layer.

3.1. Verification test 1: Multiphase conduction

We consider a variation of the multiphase planar diffusion test presented by Cleary and Monaghan [10]. The domain is a rectangle with dimensions 1.5m $\times$ 0.5m in the x and y directions, respectively. The left half of the domain is filled with air, and the right half of the domain is filled with water. The air is initially cool with a temperature of $T_g = 300$ K, and the water is one degree warmer at $T_l = 301$ K. The air properties are defined by $\rho_g = 1.275$ kg/m^3, $k_g = 0.02587$ W/m $\cdot$ K, and $c_g = 718$ J/kg $\cdot$ K, and the water properties by $\rho_l = 1000$ kg/m^3, $k_l = 0.598$ W/m $\cdot$ K, and $c_l = 4181.3$ J/kg $\cdot$ K. The top and bottom of the domain are periodic, and the left and right boundaries are adiabatic. This problem has an analytical solution for comparison, and is available for reference in the literature [10].

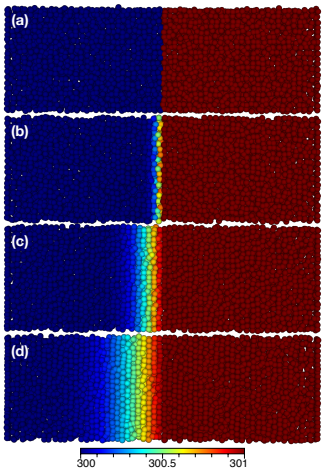

Fig. 1: Point mass particles colored by temperature (Kelvin) in the multiphase slab diffusion problem for $N_x = 60$: (a) $t = 0$s; (b) $t = 15.9$s; (c) $t = 175$s; (d) $t = 637$s.

3.1.1. Numerical specification

A uniform cartesian mesh is considered at three resolutions: $N_x = 30$ by $N_y = 10$, $N_x = 60$ by $N_y = 20$, and $N_x = 120$ by $N_y = 40$. Each mesh is made three dimensional by including three control volumes in the z direction, allowing a three-dimensional implementation to be applied to this pseudo one-dimensional test problem. Each mesh is initialized with one PMP particle per Eulerian cell, $N_{pc} = 1$. For each test, time step is set to

$$\Delta t = 0.144 \left(\Delta x\right)^2 / \alpha_l, \tag{12}$$

following prior work [10].

In order to increase the rigor of the test, we introduce a velocity $v(x)$ defined by

$$v\left(x\right) = \frac{2x_m - x}{2x_m} \frac{\Delta x}{\Delta t}, \tag{13}$$

where x_m is the center of the domain in the x direction. Introducing the velocity $v(x)$ perturbs the relative particle positions, and prevents them from assuming a steady lattice. Adding this vertical velocity does not change the analytical solution. For all cases, performance is measured via the maximum percent error, defined by

$$L_\infty(t) = \max\left[100 \times \frac{|T_i(t) - T(x,t)|}{\Delta T_o}\right], \tag{14}$$

where $\Delta T_o = T_r - T_l$ is the initial temperature difference, and $T\left(x,t\right)$ is the analytical solution, provided in [10].

3.1.2. Results

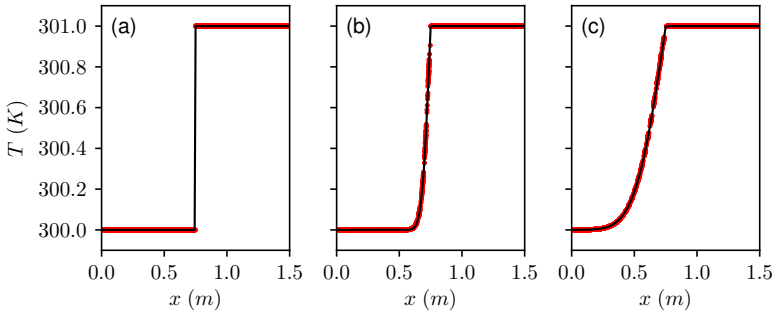

Fig. 2: Comparison of the PMP temperatures (red dots) to the analytical temperature (black line) in the multiphase slab conduction problem for $N_x = 60$: (a) $t = 0.0$s; (b) $t = 48$s; (c) $t = 637$s.

Figure 1 shows the time evolution of the PMP temperature corresponding to the $N_x = 60$ case. Initially, the gas on the left is cool, and the liquid on the right is warm. As time advances, energy diffuses into the gas and the thermal boundary layer thickens. The liquid temperature does not change visibly due to the large thermal capacitance of water relative to air. Figure 2 shows the analytical solution (black line) and the PMP temperatures (red dots) at three times for the $N_x = 60$ case. The initial temperature in panel (a) is discontinuous at the interface. At the early time of $t = 48\ s$ shown in panel (b), the PMP temperatures visually coincide with the steep gradient of the analytical solution. Close agreement continues across the boundary layer at the later time of $t = 637$ s in panel (c). Errors are quantified in Fig. 3 for the three mesh resolutions considered. Error decreases with increasing mesh resolution, and for each resolution, the errors decrease with increasing time. Errors are maximized at early times because the initial temperature gradient is large, and small perturbations of the particle position most strongly influences the error at this time.

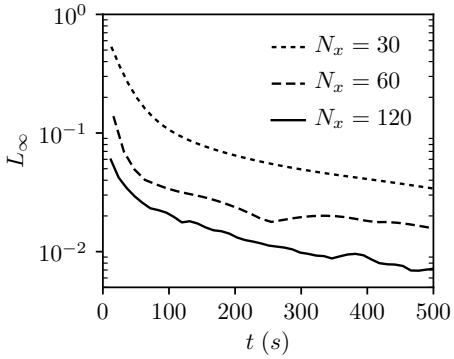

Fig. 3: Maximum percent error in the multiphase slab diffusion problem as a function of time for mesh resolutions of $N_x = 30$, $N_x = 60$, and $N_x = 120$.

3.2. Verification test 2: Advection and diffusion

The second verification considers the advection and diffusion of a Gaussian temperature profile in one-dimension. We compare the results to the analytical solution, and verify boundedness and conservation.

3.2.1. Problem setup

The problem domain is a thin tube of length $L = 1$ m in the x direction. The domain is filled with a single fluid with density $\rho = 1\ \mathrm{kg/m^3}$ and specific heat of $c = 1\ \mathrm{J/kg \cdot K}$. Thermal conductivity is considered at values of $\mathrm{k} = 0.002\ \mathrm{W/m \cdot K}$ and $\mathrm{k} = 0.0\ \mathrm{W/m \cdot K}$, providing high and low diffusivity cases. The fluid travels from left to right with a speed of $u_o = 1$ m/s. The temperature is initialized with a Gaussian distribution defined by

$$T(x, t_o) = T_o + A \times \exp\left(-\frac{(x/L - x_o/L)^2}{\sigma^2}\right), \quad (15)$$

where $T_o = 300$ K, $A = 50$ K, $x_o = 1/8$ m, and $\sigma = 0.04$. With periodic boundary conditions, the analytical solution to this problem is given by

$$T(x,t) = T_o + \frac{A}{\sqrt{1 + (4\mathrm{k}t/L^2)/\sigma^2}} \times \exp\left(-\frac{((x/L - u_o t/L) - x_o/L)^2}{\sigma^2 + 4\mathrm{k}t/L^2}\right). \quad (16)$$

3.2.2. Numerical parameters

The mesh is defined by $N_x = 90$, and $N_y = N_z = 3$. One PMP particle is initialized in every computational cell, $N_{pc} = 1$. For the low diffusivity case ($\mathrm{k} = 10^{-12}\ \mathrm{W/m \cdot K}$), the time step is defined by

$$\Delta t = \frac{u_o}{\Delta x}, \quad (17)$$

and for the high diffusivity case ($\mathrm{k} = 0.002\ \mathrm{W/m \cdot K}$) the time step is defined by

$$\Delta t = 0.144\,(\Delta x)^2/\alpha. \quad (18)$$

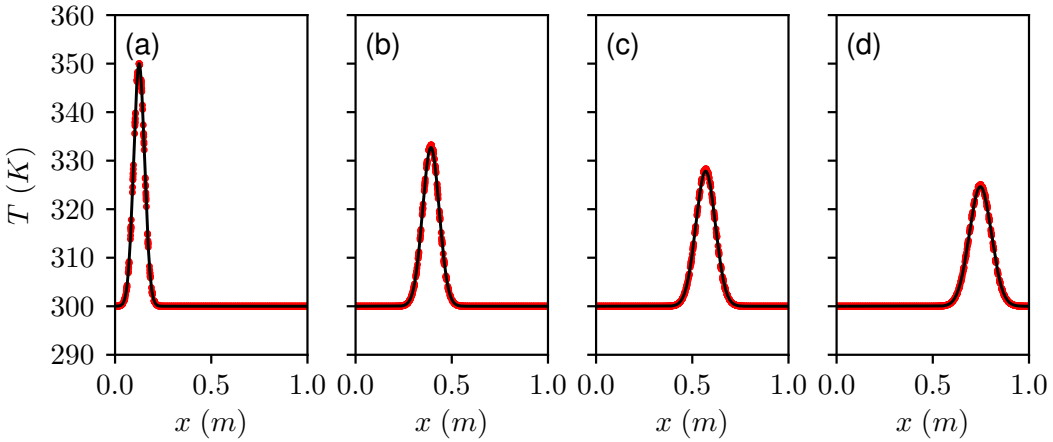

Fig. 4: Temporal evolution of the PMP temperatures (red dots) and the analytical temperature (black line) for the high diffusivity Gaussian: (a) $t = 0.0$; (b) $t = 0.267$; (c) $t = 0.444$; (d) $t = 0.622$.

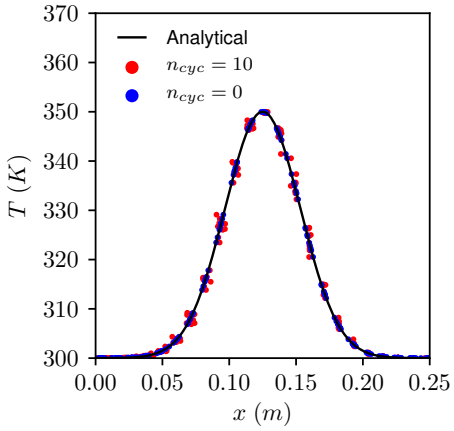

Fig. 5: Temperature profile for the low diffusivity Gaussian at the initial state (blue dots, $n_{cyc} = 0$) and after ten flow-through times (red dots, $n_{cyc} = 10$). Analytical solution shown by black line.

The y direction velocity applied to the multiphase diffusion tests is applied to the Gaussian tests.

3.2.3. Results

Figure 4 shows the PMP temperatures as a function of time for the high diffusivity Gaussian. Initially, the temperature gradient is large near $x = 1/8$. As the fluid flows from left to right, the energy diffuses, smoothing the gradient and decreasing the maximum temperature. For all times, the PMP temperatures (red) are in good agreement with the analytical solution (black). The result is bounded and conservative to machine precision.

Performance of the low diffusivity Gaussian is assessed by allowing the flow to recirculate through the domain for ten cycles, $n_{cyc} = 10$. As there is no diffusion, the Gaussian profile should return to its initial condition. Results of the low diffusivity Gaussian are shown in Fig. 5. The initial PMP temperatures, shown as blue dots, are coincident with the analytical solution, shown as the black line. The PMP temperatures after ten flow through times, shown as red dots, are no longer in perfect agreement with the analytical solution, but show superior performance relative to Eulerian advection schemes. The error is introduced by the small-scale shifting of the PMP particles. Like the high diffusivity Gaussian, this result is bounded and conservative.

3.3. Demonstration problem 1: Rising gas bubble

We consider a hot gas bubble rising in a cool liquid. The initial problem configuration is illustrated in Fig. 6. The $R = 0.61$ cm gas bubble is initially hot at $T_g = 500$ K, and the liquid is cool at $T_l = 300$ K. Liquid and gas properties are defined by $\rho_l = 875.5\ \mathrm{kg/m^3}$, $\rho_g = 1\ \mathrm{kg/m^3}$, $\mu_l = 0.118\ \mathrm{Pa \cdot s}$, $\mu_g = 0.001\ \mathrm{Pa} \cdots$, and the surface tension coefficient is $\sigma = 0.0322\ \mathrm{N/m}$. All boundaries are periodic, and gravity acts in the $-z$ direction. This configuration is similar to the experiments conducted by Hnat and Buckmaster [12], and the numerical simulation done by Sussman and Smereka [13].

3.3.1. Numerical specification

The simulation is performed on a $128 \times 256 \times 128$ mesh with $N_{pc} = 2$ particles per Eulerian cell. Results are presented using in the following nondimensional expressions:

$$T^{\star} = \frac{T - T_g}{T_l - T_g}; \tag{19}$$

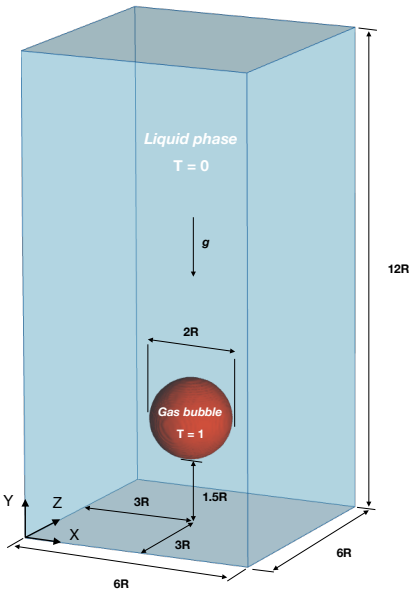

Fig. 6: Flow configuration for rising bubble demonstration problem.

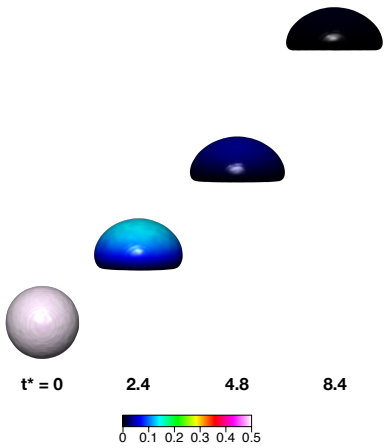

Fig. 7: Bubble surface colored by dimensionless temperature as it rises through cool liquid.

and

$$t^\star = (v_\infty / L)t, \tag{20}$$

where v_∞ is the steady rise speed of the bubble.

3.3.2. Results

The liquid/gas interface colored by the temperature is shown as a function of time in Fig. 7. The bubble slowly deforms from its initially spherical shape as it rises through the liquid. Significant deformation occurs by $t^\star = 2.4$, and a steady geometry is achieved by time $t^\star = 6$. The interface temperature is uniformly warm initially, and cools as the bubble rises through the liquid. Cooling occurs more rapidly on the bottom of the bubble than the top, and the interface achieves a uniformly cool profile by $t^\star = 8.4$. The steady rise speed of the bubble is $21.9\ \mathrm{cm/s}$, which agrees with the $21.9\ \mathrm{cm/s}$ identified via simulation by Sussman and Smereka [13], as well as the experimentally measured speed of $21.5\ \mathrm{cm/s}$ by Hnat and Buckmaster [12].

3.4. Demonstration problem 2: Temporal mixing layer

The final problem is a temporal mixing layer. The purpose of this demonstration is to examine the ability of the method to provide low dissipation, bounded results for scalar transport in the context of turbulent flows. The mixing layer is defined by $Re = \gamma\delta_{\omega_o}/\nu = 140,000$ and $Pr = 0.5$, where ν is the kinematic viscosity, γ is the free-stream velocity difference, and δ_{ω_o} is the initial vorticity thickness. A standard hydrodynamic initialization is applied [14] where the fluid at the top of the domain moves to the right and the fluid at the bottom of the domain moves to the left. Perturbations are added to the initial velocity field to expedite the growth of the hydrodynamic instabilities and reduce the simulation time [15]. The temperature is initialized *discontinuously*, with the top half set to $300\ \mathrm{K}$ and the bottom half to $400\ \mathrm{K}$.

3.4.1. Numerical parameters

The computational domain is discretized by $192 \times 192 \times 3$ computational nodes in the x, y, and z directions, respectively, and each cell is initialized with $N_{pc} = 2$ particles. The flow field is intentionally under-resolved. The purpose of this demonstration is to examine the numerical dissipation of the method, and to verify boundedness of the temperature.

3.4.2. Results

The mixing layer temperature is shown on the Eulerian mesh in Fig. 8 at four times, increasing from left to right. The initially thin boundary layer is apparent in panel (a), and remains thin in panel (b). Significant development and mixing has occurred by panel (c), and the length scales of the temperature field have decreased significantly. At the final time in panel (d), the smallest length scales have continued to grow smaller. While much of the vortex region is characterized by the intermediate temperature, the full spectrum of temperatures remains present in the vortex cores – this result is made possible by the low dissipation and bounded transport of the ELPMP method.

An assessment of the ELPMP performance can be made by comparison to a widely used method, such as the BQUICK scheme [5]. This comparison is presented in Fig. (9), where the BQUICK result appears in panel (a) and the ELPMP result appears in panel (b). The ELPMP result presents considerably less numerical dissipation, while preserving boundedness without limiters.

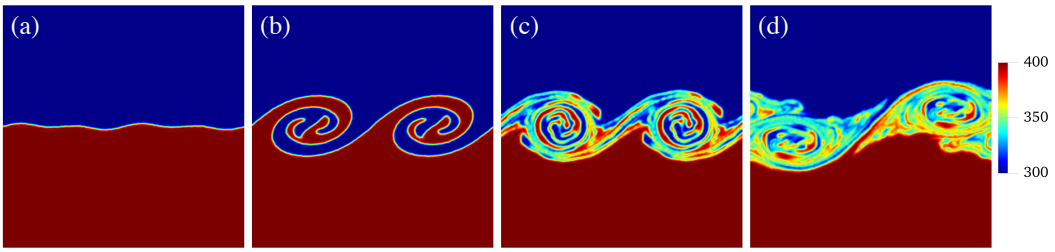

Fig. 8: Temperature contours in a temporal mixing layer (Kelvin): (a) $t = 0.59$; (b) $t = 4.93$; (c) $t = 13.97$; and (d) $t = 20.93$.

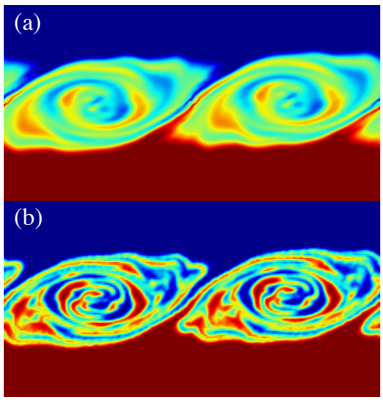

Fig. 9: Comparison of temperature contours in the temporal mixing layer at $t = 16.3$ produced by: (a) the BQUICK scheme, and (b) the ELPMP scheme.

4. Conclusion

We have presented a method for performing scalar transport in the ELPMP framework. Diffusion is achieved though a modified smoothed particle hydrodynamics diffusion operator [10], while scalar advection is accounted for by the motion of the point mass particles. Verification tests for interfacial diffusion and single phase advection-diffusion show the method to provide low–dissipation, bounded, and conservative scalar transport. Robustness of the method has been demonstrated by simulating a gas bubble rising in liquid, and a high Reynolds number mixing layer. Coupled with previously demonstrated phase tracking performance [6], these results suggest the ELPMP may be a valuable tool for the modeling and simulation of spray combustion.

Acknowledgments

Sandia National Laboratories is a multi-mission laboratory managed and operated by National Technology and Engineering Solutions for Sandia LLC, a wholly owned subsidiary of Honeywell International, Inc., for the U.S. Department of Energy's National Nuclear Security Administration under contract DE-NA0003525.

References

[1] B. Abramzon, W. Sirignano, Droplet vaporization model for spray combustion calculations, Int. J. Heat Mass Trans. 32 (9) (1989) 1605 – 1618.

[2] S. R. Sarkar S, Direct numerical simulation of heat transfer in spray cooling through 3d multiphase flow modeling using parallel computing, J. Heat Trans. 131 (12) (2009) 121007–121007.

[3] M. Rudman, A volume-tracking method for incompressible multifluid flows with large density variations, Int. J. Numer. Meth. Fl. 28 (1998) 357–378.

[4] M. Owkes, O. Desjardins, A mass and momentum conserving unsplit semi-Lagrangian framework for simulating multiphase flows, J. Comp. Phys. 332 (2017) 21–46.

[5] M. Herrmann, G. Blanquart, Flux corrected finite volume scheme for preserving scalar boundedness in reacting large-eddy simulations, AIAA Journal 44 (12) (2006) 2879–2886.

[6] E. Wenzel, S. Garrick, A point-mass particle method for the simulation of immiscible multiphase flows on an Eulerian grid, J. Comp. Phys. 387 (2019) 108835.

[7] E. Wenzel, S. Garrick, Modeling and Simulation of Turbulent Mixing and Reaction, Springer Singapore, 2020, Ch. A Coupled Eulerian-Lagrangian Framework for the Modeling and Simulation of Turbulent Multiphase Flows, pp. 227–250.

[8] M. B. Liu, G. R. Liu, Smoothed particle hydrodynamics (SPH): an overview and recent developments, Arch. Comput. Methods Engrg. 17 (1) (2010) 25–76.

[9] D. J. Price, Smoothed particle hydrodynamics and magnetohydrodynamics, J. Comp. Phys. 227 (3) (2012) 759–794.

[10] P. Cleary, J. Monaghan, Conduction Modelling Using Smoothed Particle Hydrodynamics, J. Comp. Phys. 148 (1999) 227–264.

[11] J. Monaghan, Smoothed particle hydrodynamics, Ann. Rev. Astron. Astrophys. 30 (1992) 543–574.

[12] J. G. Hnat, J. D. Buckmaster, Spherical cap bubbles and skirt formation, Phys. Fluids 19 (2) (1976) 182–194.

[13] M. Sussman, P. Smereka, Axisymmetric free boundary problems, J. Fluid Mech. 341 (1997) 269–294.

[14] R. W. Metcalfe, S. A. Orszag, M. E. Brachet, S. Menon, J. J. Riley, Secondary instability of a temporally growing mixing layer, J. Fluid Mech. 184 (1987) 207–243.

[15] R. T. Pierrehumbert, S. E. Widnall, The two and three dimensional instabilities of a spatially periodic shear layer, J. Fluid Mech. 114 (1982) 59–82.